



## Effects of Ambient Oxygen and Density on Primary Soot Size under Diesel-Like Conditions Using a Lagrangian Soot Tracking Model

Ong, Jiun Cai; Pang, Kar Mun; Walther, Jens Honore; Ho, Jee-Hou; Ng, Hoon Kiat

*Published in:*

S A E International Journal of Engines

*Link to article, DOI:*

[10.4271/03-14-02-0018](https://doi.org/10.4271/03-14-02-0018)

*Publication date:*

2021

*Document Version*

Peer reviewed version

[Link back to DTU Orbit](#)

*Citation (APA):*

Ong, J. C., Pang, K. M., Walther, J. H., Ho, J-H., & Ng, H. K. (2021). Effects of Ambient Oxygen and Density on Primary Soot Size under Diesel-Like Conditions Using a Lagrangian Soot Tracking Model. *S A E International Journal of Engines*, 14(2), 301-315. <https://doi.org/10.4271/03-14-02-0018>

---

### General rights

Copyright and moral rights for the publications made accessible in the public portal are retained by the authors and/or other copyright owners and it is a condition of accessing publications that users recognise and abide by the legal requirements associated with these rights.

- Users may download and print one copy of any publication from the public portal for the purpose of private study or research.
- You may not further distribute the material or use it for any profit-making activity or commercial gain
- You may freely distribute the URL identifying the publication in the public portal

If you believe that this document breaches copyright please contact us providing details, and we will remove access to the work immediately and investigate your claim.

# 1 **Effects of Ambient Oxygen and Density on Primary Soot Size under Diesel-** 2 **like Conditions using a Lagrangian Soot Tracking Model**

## 3 **Abstract**

4 This paper investigates the effect of ambient oxygen levels and ambient density on the  
5 primary soot size under diesel engine-like conditions via a Lagrangian soot tracking (LST)  
6 method. The numerical studies and soot analysis are carried out for an *n*-heptane spray flame  
7 in the Sandia constant volume combustion chamber. Numerical studies are carried out at two  
8 oxygen levels of 15% and 12%, as well as two ambient densities of 14.8 kg/m<sup>3</sup> and 30 kg/m<sup>3</sup>.  
9 The LST model involves treating the soot particles formed in the spray flame as Lagrangian  
10 particles and their individual soot information are stored. Based on the primary soot size  
11 distribution for soot particles in the core of the spray jet, an increase in ambient density from  
12 14.8 kg/m<sup>3</sup> to 30 kg/m<sup>3</sup> is shown to increase the peak and mean soot size by a factor of 1.5.  
13 Furthermore, the peak and mean primary soot size decreases with decreasing oxygen levels  
14 from 15% to 12%. The larger primary soot at higher oxygen levels and ambient densities can  
15 be attributed to the higher net growth rate experienced by the soot particles. At low density,  
16 the span of soot cloud is shorter at low oxygen level. In contrast, the high density cases show  
17 comparable soot cloud span for both oxygen levels before steady-state is reached. Soot age is  
18 introduced to predict the soot residence time in the spray flame. The results show that soot  
19 residence time is dependent on both the span of the soot cloud and the initial onset location of  
20 the soot formed.

21 **Keywords:** Lagrangian soot tracking; primary soot; soot age; soot size; diesel spray

## 22 **1. Introduction**

23 Soot is one of the most distinctive and problematic emissions of diesel engines due to its  
24 complex formation and oxidation processes. Soot particles are normally formed as fractal  
25 open structured agglomerates with large quantities of nano-sized primary particles via  
26 incomplete combustion of hydrocarbon fuels [1,2]. The morphological characteristics and  
27 nanostructural properties of combustion-generated soot particles are of paramount importance  
28 because they are closely linked to the formation of primary soot particles and soot oxidative  
29 reactivity [3]. Furthermore, ultrafine particle emissions from incomplete combustion are  
30 harmful to human health [4,5]. This concern has led to the legislation of Euro 5/6 which aims  
31 to reduce soot mass and particle number emissions [6,7]. Driven by the stringent legislations  
32 for pollutant emissions, detailed analysis of soot morphology and its evolution could provide  
33 useful insights into mitigating the detrimental impact of particle emissions.

34 Transmission Electron Microscopy (TEM) analysis of soot particles directly sampled  
35 from a diesel spray flame has emerged to be a powerful and quantitative technique for  
36 studying soot particle size. This direct soot sampling technique has been successfully applied  
37 in reacting diesel jets, under high-pressure and high-temperature ambient conditions for soot  
38 study in a constant volume vessel [8–14], as well as in diesel engines [15–17]. Kook and  
39 Pickett [8] studied the morphology of soot particles extracted from diesel spray flames at  
40 ambient temperature and density of 1000 K and 6.7 MPa, respectively in a constant volume  
41 vessel by using a thermophoretic probe. The TEM analysis of the soot samples along  
42 different in-flame axial locations revealed that the diameters of primary soot increase at first,  
43 reach a peak and then decrease [8], in which the decrease in primary soot size is due to soot  
44 oxidation. Several studies [9,18] showed similar trend. Similar sampling technique and TEM  
45 analysis were used by Kuribayashi et al. [14] to study the effects of oxygen (O<sub>2</sub>) level (15%  
46 and 21%) on soot concentration, size, number density and morphology in a diesel spray

47 flame. They found that lowering the ambient oxygen concentration resulted in a delayed and  
48 downstream-shifted soot processes, as well as an increase in the aggregate size in the  
49 downstream region. However, the primary soot size remained relatively stable when the  
50 oxygen concentration decreased from 21% to 15%. Besides this work, the same approach  
51 (direct sampling and TEM analysis) has also been applied in other studies, such as fuel  
52 comparison among conventional diesel, biodiesel and Fischer-Tropsch Diesel [11,12], effect  
53 of injected fuel amount [17], and nanostructure analysis of primary particles [19,20]. Despite  
54 successful implementation in various studies, a major limitation of the direct soot sampling  
55 and TEM analysis is the time resolution. Since the thermophoretic probe is constantly  
56 exposed to the diesel flame, the sampled soot is a time-integrated mixture of soot particles  
57 throughout the injection and combustion duration. Therefore, the use of computational fluid  
58 dynamics (CFD) is expected to overcome the limitations of TEM analysis of sampled soot by  
59 giving instantaneous spatial or temporal information of the soot formation process.

60         There are a few methods available for CFD analysis that can model soot size  
61 distribution. One approach is the Method of Moments (MOM) [21], in which the evolution  
62 equations for moments of the population distribution are solved instead of explicitly solving  
63 the population distribution [22]. MOM was used by Ito et al. [23] who compared the  
64 predicted primary soot size from MOM against the measurement data from a laser-induced  
65 incandescence experiment of *n*-heptane spray combustion in a constant volume chamber.  
66 Recently, Naik et al. [24] utilized MOM in their simulation study of high-pressure lifted  
67 flames in a constant-volume chamber. In addition to *n*-heptane fuel, a two-component  
68 surrogate fuel, conventional U.S. No. 2 diesel (D2), and world-averaged jet fuel (Jet-A) were  
69 considered in their simulation study [24]. Another approach is the discrete sectional method  
70 (DSM) [25–27] which discretizes the population of soot particles into discrete sections or  
71 “bins” and the evolution equations are solved for each of these bins. This method has been

72 applied to model primary soot size distribution in optical engine [28,29]. It is important to  
73 note that MOM only predicts ensemble averaged quantities where the exact shape of the  
74 particle size distribution is unknown. As for DSM, in order to achieve good accuracy, a  
75 higher number of sections is needed to represent the particle size distribution, thus making it  
76 computationally expensive. It is also noteworthy that both MOM and DSM can only provide  
77 the mean primary particle soot size, and do not provide information about the history of the  
78 soot particles which may contain vital information to understand the soot processes.

79         The Lagrangian tracking method is an alternative to DSM and MOM for computing  
80 particle dynamics. It allows the possibility to track an individual particle continuously along  
81 its trajectory, and to monitor its individual interaction with both the gas phase and the other  
82 particles. No classes or sections of particles are required, thus making the calculation of the  
83 particle size distribution relatively straightforward. Gallen et al. [30] introduced a semi-  
84 deterministic Lagrangian particle tracking methodology that tracks the Lagrangian soot  
85 particles as well as consider their collision process. A hybrid Eulerian-Lagrangian method for  
86 soot modelling, which was developed by Dellinger et al. [31], combined a reduced gas-phase  
87 chemistry, a sectional model for polycyclic aromatic hydrocarbons, and a Lagrangian  
88 description of soot particles dynamics. The Lagrangian soot particles were nucleated from  
89 polycyclic aromatic hydrocarbons molecules and radicals. Meanwhile, two-way coupling of  
90 the gaseous and solid phases was assumed. It is important to note that the aforementioned  
91 studies were both related to gas turbine applications. A Lagrangian soot tracking (LST)  
92 model based on a semi-empirical formulation was recently developed by Ong et al. [32] and  
93 was successfully implemented for diesel spray applications. The LST model was validated  
94 using the experimental data of *n*-dodecane and *n*-heptane spray flame from the Engine  
95 Combustion Network. Despite omitting the coagulation process, the LST model was

96 demonstrated to be able to predict primary soot size, track individual soot particles, and  
97 access their history as they evolve in the diesel spray flame.

98         Setting against this background, the present study is carried out by integrating the  
99 previously developed LST model [32] with a reduced *n*-heptane chemical mechanism to  
100 investigate the effect of ambient oxygen and density on primary soot size in a Sandia *n*-  
101 heptane reacting spray. The paper is structured such that numerical formulation and setup are  
102 first provided. This is followed by the validation of CFD models using non-reacting and  
103 reacting spray experimental data. The validation of the LST method is carried out by  
104 comparing the distribution of the steady-state soot volume fraction (SVF). Following this is  
105 the study of soot size distribution for soot particles formed at the core of the jet during the  
106 transient and the steady-state phase.

## 107 **2. Numerical formulation and setup**

### 108 **2.1 Mesh and numerical models**

109 The computational study was performed using the spray combustion solver in an open-source  
110 code, OpenFOAM version 2.0.x [33]. Experimental data from the Sandia combustion vessel  
111 [34] was used for the model validation of the *n*-heptane spray and its combustion  
112 characteristics. Detailed descriptions of the experimental setup are available in [34]. The  
113 constant volume combustion vessels were represented by a cylinder during simulation  
114 studies. For computational expediency, the cylindrical chamber was simplified to a 4-degree  
115 axisymmetric wedge with a single layer of cells in the tangential direction. Details of the  
116 mesh and geometry can be found herein [32]. The time step size was fixed at 0.2  $\mu$ s. The non-  
117 reacting spray case was studied at an ambient temperature of 1000 K and ambient density of  
118 14.8 kg/m<sup>3</sup> with the absence of oxygen (0% O<sub>2</sub> in ambient gas composition). As for the  
119 reacting spray case, there were a total of four cases with two oxygen concentrations (15% and

120 12%) and two ambient densities ( $14.8 \text{ kg/m}^3$  and  $30 \text{ kg/m}^3$ ), while having the same initial  
121 ambient temperature of 1000 K. Cases with ambient density of  $14.8 \text{ kg/m}^3$  and  $30 \text{ kg/m}^3$  were  
122 henceforth addressed as low density and high density cases, respectively for brevity. Injection  
123 specifications and profiles in the current simulations were set to correspond to those used in  
124 the experimental setup. Details of the experimental conditions and the injection parameters  
125 are shown in Table 1.

126 The spray breakup was described using the Reitz-Diwakar model [35]. The model  
127 constant that governs the time factor for stripping,  $C_s$  was set to 11.5. The turbulent flow was  
128 modelled using the Unsteady Reynolds Averaged Navier-Stokes (URANS) method with the  
129 standard  $k - \varepsilon$  model [36]. The model constant  $C_{1\varepsilon}$  was calibrated according to its  
130 approximation of round jets [37, 38] and set to a value of 1.53. The initial turbulence kinetic  
131 energy,  $k$  was set to  $0.735 \text{ m}^2/\text{s}^2$ , which was estimated based on the measured RMS velocity  
132 in the experiment [34]. The initial turbulence dissipation rate,  $\varepsilon$  was set to  $5.67 \text{ m}^2/\text{s}^3$  based  
133 on the turbulence integral length scale of 0.01 mm. The choice of the initial  $k$  and  $\varepsilon$  are  
134 similarly used in Ref. [38, 39, 40]. The average velocity in the combustion chamber prior to  
135 spray injection is approximately 0.7 m/s as provided in ECN [34]. This gas velocity is too  
136 low to cause significant effect on the spray development as the spray velocity is 400 – 600  
137 m/s. Therefore, the initial velocity field for all cases was set to be zero. Similar treatment of  
138 the initial velocity field can be seen in Ref. [39]. Soot radiation modelling was neglected in  
139 all test cases [41]. Collision and coalescence with the fuel spray region were omitted in all  
140 studies as these processes have negligible influence on the liquid and vapour fuel penetration  
141 of evaporating spray [42]. In addition, the Ranz-Marshall correlation [43] was implemented  
142 to calculate the droplet heat transfer with the surrounding gas phase while the Frossling  
143 correlation [44] was used to model the evaporation of droplet fuel. The skeletal *n*-heptane  
144 mechanism developed by Pang et al. [45] was implemented to describe the chemical kinetics

145 of *n*-heptane spray combustion. Details about the mechanism can be referred to in [45]. In  
146 this current study, the spray combustion solver was incorporated with a LST model [32]. The  
147 LST model is explained in detail in our previous study [32] but for completeness the essential  
148 features are outlined here.

## 149 **2.2 LST model for soot particles**

150 The LST model treats soot particles as Lagrangian particles and they are tracked via the  
151 Lagrangian method, in which the motion of the soot particles are computed using Newton's  
152 second law of motion. The dispersion of Lagrangian particles due to turbulence is influenced  
153 by the instantaneous fluctuating velocity  $\vec{u}'$  [46, 47], which is modelled by the discrete  
154 random walk model (DRW) [46, 47]. It correlates with the flow turbulent kinetic energy  $k$ ,  
155 predicted by the standard  $k - \varepsilon$  model, and is expressed by

$$\vec{u}' = \zeta \sqrt{2k/3} \begin{Bmatrix} 1 \\ 1 \\ 1 \end{Bmatrix} \quad (1)$$

156 where  $\zeta$  is a Gaussian random number [45,46] with zero mean and unit variance.

157 The LST model also considers the inception, surface growth and oxidation processes  
158 of the soot particles. It is important to note that the coagulation process is omitted in the LST  
159 model as the surface growth is the relatively dominant process in affecting primary soot  
160 particle size [48, 49]. The inception, surface growth and oxidation rates in the LST model are  
161 adapted from the semi-empirical, multi-step Moss-Brookes (MB) soot model [50]. The MB  
162 soot model is chosen due to its flexibility in implementing different surface ageing model, as  
163 shown in Ref. [51].

164 The inception rate,  $\omega_{inc}$  is given by

$$\omega_{inc} = C_{inc} M_P \left( \frac{X_{prec} P}{RT} \right) \exp \left\{ - \frac{T_{inc}}{T} \right\} \quad (2)$$



165 where  $X_{prec}$  denotes the mole fraction of soot precursor, whereas  $C_{inc}$  is the model constant  
 166 for soot incipient rate and is given as  $54 \text{ s}^{-1}$ .  $T$ ,  $P$  and  $R$  denote the gas temperature, pressure  
 167 and universal gas constant, respectively. The activation temperature of soot inception,  $T_{inc}$  is  
 168 given as 21,000 K. The constant  $M_p$  represents the mass of an incipient soot particle which is  
 169 set to 1200 kg/kmol. In the LST model, Lagrangian particles are formed when a formation  
 170 criterion in a computational cell is met. The formation criterion at cell  $j$  is given as

$$m_{inc,j} > m_{inc,min} \quad (3)$$

171 where  $m_{inc,j}$  denotes the total incipient soot mass at cell  $j$  and  $m_{inc,min}$  denotes the minimum  
 172 mass of incipient soot.  $m_{inc,j}$  is calculated by taking the product of  $\omega_{inc,j}$  and the time-step  
 173  $\Delta t$ . Meanwhile,  $m_{inc,min}$  is calculated to be  $2.0 \times 10^{-24}$  kg, based on the assumption that the  
 174 minimum diameter of an incipient soot is 1.24 nm [52], with the soot density of  $2000 \text{ kg/m}^3$   
 175 [52, 53]. The single formed Lagrangian particle is assumed to represent the total number of  
 176 incipient soot particles in that particular computational cell at that time instance. It is also  
 177 assumed that all particles formed in that cell, at that instant, follow the same pathway [54]  
 178 and size change as the existing Lagrangian particle. The initial velocity of the new particle  
 179 formed follows the mean velocity of the cell it is formed in.

180 The newly formed Lagrangian particles then undergo mass addition and increase in  
 181 size through the surface growth process and decrease in size due to oxidation processes via  
 182 hydroxyl radicals (OH) and  $\text{O}_2$ . The rate of change of soot diameter due to surface growth is  
 183 governed by Equation (4), whereas the diameter change due to oxidation is by Equation (5)  
 184 and (6).

$$\left. \frac{d}{dt} (d_i) \right|_{SG} = \alpha \left[ 2C_{sg} \left( \frac{X_{sg}P}{RT} \right) \frac{1}{\rho_{soot}} \exp \left\{ -\frac{T_y}{T} \right\} \right] \quad (4)$$

$$\left. \frac{d}{dt} (d_i) \right|_{ox \text{ via } OH} = 2C_{OH} \eta_{coll} \left( \frac{X_{OH}P}{RT} \right) \frac{\sqrt{T}}{\rho_{soot}} \quad (5)$$

$$\left. \frac{d}{dt} (d_i) \right|_{ox \text{ via } O_2} = 2C_{O_2} \left( \frac{X_{O_2}P}{RT} \right) \frac{\sqrt{T}}{\rho_{soot}} \exp \left\{ -\frac{T_{O_2}}{T} \right\} \quad (6)$$

185 The mole fraction surface growth species is denoted as  $X_{sg}$ . The mole fractions for  
 186 soot oxidants, OH and O<sub>2</sub> are represented by  $X_{OH}$  and  $X_{O_2}$ , respectively. It is important to  
 187 note that acetylene (C<sub>2</sub>H<sub>2</sub>) is chosen here as the surface growth species and soot precursor  
 188 species. Although polycyclic aromatic hydrocarbon is also an important soot precursor. To  
 189 accurately predict the formation of PAH, a larger chemical mechanism that includes PAH  
 190 formation pathways is required, which will incur higher computational cost. Furthermore,  
 191 numerous numerical studies of soot formation in diesel spray flame consider only acetylene  
 192 as soot precursor, e.g. Ref. [38, 55-57]. Therefore, only acetylene is chosen as the soot  
 193 precursor to achieve a balance of accuracy and computational efficiency. Furthermore, one-  
 194 way coupling is assumed between the Lagrangian soot particles and the gaseous species. This  
 195 implies that the gaseous species affects the Lagrangian soot particles but not the other way  
 196 around. The soot model constants, their descriptions and values are shown in Table 2. The  $\alpha$   
 197 in Equation (4) denotes the surface ageing factor, which is assumed to be a function of  
 198 temperature and is expressed as

$$\alpha = \frac{1}{2} \left( \tanh \left( \frac{8168}{T} - 4.57 \right) + 1 \right) \quad (7)$$

199 Once a Lagrangian soot particle is reduced below a threshold diameter, it is assumed to be  
 200 fully oxidised and is removed from the computational cell. The threshold value is set to 1.24  
 201 nm which is the same as the initial incipient soot particle size.

## 202 **3. Results and discussion**

### 203 **3.1 Validation of numerical models**

204 The first part of this section compares the simulation results of non-reacting fuel spray  
205 against experimental measurements, in terms of liquid and vapour penetration lengths as well  
206 as the mixture fraction. It is followed by the validation of the computed ignition delay times  
207 (IDT) and lift-off lengths (LOL) of reacting sprays using the experimental data [34]. The  
208 non-reacting and reacting spray validation cases are carried out to ensure that the fuel-air  
209 distribution and combustion characteristics are reasonably simulated, and the uncertainties  
210 induced by these elements can be minimised prior to studying soot formation events. The  
211 validation of LST model is carried out by comparing the predicted SVF profiles with  
212 measured data during steady-state combustion for different ambient conditions.

213 In the current work, the liquid penetration length (LPL) is taken as the axial location  
214 from the injector to the location where 99% of the total liquid mass is found, while the vapour  
215 penetration length (VPL) is taken as the maximum distance from the nozzle outlet to where  
216 the fuel mass fraction (or mixture fraction) is 0.1%. As for the LOL, it is defined as the first  
217 axial location of Favre-averaged OH mass fraction which reaches 2% of its maximum value  
218 in the domain. The time averaging of the simulated LOL is carried out from 3.0 to 6.0 ms.  
219 This corresponds to the experimental definition. The IDT is defined as the time when the  
220 greatest rise of maximum temperature is observed,  $\left(\frac{dT_{max}}{dt}\right)_{max}$ , and this definition remains  
221 consistent throughout the study. Although there are other definitions for the IDT, it is shown  
222 that there is no significant discrepancy in the IDT between different IDT definitions [39].  
223 Moreover, this definition is in accordance with the recommendation by the Engine  
224 Combustion Network [34].

### 225 3.1.1 Non-reacting spray simulations

226 Comparisons between the computed and measured penetration lengths are provided in Figure  
227 1(a) using the default and calibrated model constant. In general, the tuned model shows an  
228 improved VPL and LPL prediction as compared to the measurement. Computed and  
229 measured mean radial mixture fraction profiles are next compared in Figure 1(b). The overall  
230 trend of the mixture fraction profiles agrees with the experimental data which implies that the  
231 air-fuel distributions are reasonably predicted by the model.

### 232 3.1.2 Reacting spray simulations

233 Figure 2 shows the comparison of experimental and predicted IDT/LOL for the reacting *n*-  
234 heptane spray cases at different oxygen levels and ambient densities. At low density, the  
235 predicted IDTs correspond well with the measured IDT for 15% and 12% oxygen levels with  
236 a maximum relative difference of 7.3%. A maximum relative difference of 17.5% is obtained  
237 for the predicted IDT at a higher ambient density of 30.0 kg/m<sup>3</sup>. At high density (30.0 kg/m<sup>3</sup>),  
238 the predicted LOLs at both oxygen levels are within a relative difference of 7% as compared  
239 to the experimental LOL. At low density (14.8 kg/m<sup>3</sup>), the predicted LOL at 12% O<sub>2</sub> and  
240 15% O<sub>2</sub> are underpredicted by 6% and 20%, respectively. Nevertheless, the simulated LOLs  
241 are shown to correspond well with the measured data for all the reacting spray cases by  
242 capturing the LOL trend, where the LOL increases with increasing ambient density and  
243 decreasing oxygen levels.

### 244 3.1.3 Steady-state SVF distribution

245 In this section, the predicted SVF results using the LST model are compared against the  
246 measured SVF for different oxygen concentrations and ambient densities. The experimental  
247 SVF are obtained from the time-averaged line-of-sight extinction (KL) data [34]. Predicted  
248 SVF using the LST model is calculated based on the total number of Lagrangian soot  
249 particles in the domain. Figure 3 shows the temporal evolution of the number of

250 computational particles for soot under different ambient densities and oxygen levels. It is  
251 depicted in the figure that the number of soot particles reaches a quasi-steady state at  $t \geq 4$   
252 ms. Therefore, the predicted steady-state SVF using the LST model is obtained by time-  
253 averaging the computed SVF from 4 – 6 ms. In addition, normalization is carried out by  
254 normalizing the simulated and measured SVF with their respective peak SVF at 15% O<sub>2</sub>, 30.0  
255 kg/m<sup>3</sup> density. The normalized SVF profiles for different oxygen levels and ambient densities  
256 along the spray axis are shown in Figure 4. The simulated SVF for the 12% O<sub>2</sub>, 30.0 kg/m<sup>3</sup>  
257 density case is underpredicted by approximately 30% relative to the measured data. At low  
258 density, the predicted SVF at 15% O<sub>2</sub> is overpredicted by a factor of two as compared to the  
259 measured result. The larger discrepancy at 15% O<sub>2</sub> is likely due to the underpredicted LOL  
260 which leads to less air entrainment into the spray and subsequently higher soot formation (cf.  
261 Figure 2). Despite these discrepancies, the predicted SVF using the LST model is shown to  
262 increase with increasing oxygen level and ambient density, which corresponds with the  
263 experimental observation as depicted in Figure 4. The spatial location of the predicted SVF is  
264 further downstream than the measured SVF. This can be attributed to the use of the Moss-  
265 Brookes soot model in the formulation of the LST model which is discussed in [32]. It is  
266 shown in Ref. [39] that considering surface ageing effect in the surface growth model can  
267 cause the spatial location of the soot cloud to be more upstream. Therefore, it is expected that  
268 implementing a more advanced surface ageing model than the one implemented in the  
269 present study will likely improve the spatial prediction of the LST model. Despite the  
270 overprediction, the LST model is able to capture the variation of spatial location of SVF  
271 towards the upstream location of the spray as oxygen level increases and ambient density  
272 increases, which coincides with experimental observation (cf. Figure 4). It is important to  
273 note that a single simulation case using the LST model requires approximately 170 hours to

274 reach 6.0 ms after start of fuel injection when running in serial on a HP Z200 Workstation  
275 with Quad-Core Intel Xeon Processor 3400 at 2.40 GHz.

## 276 **3.2. In the spray core jet**

### 277 *3.2.1 Sampling of individual lagrangian soot particles*

278 The soot sampling experiment was conducted by Aizawa and colleagues, in which full details  
279 of the experimental methodology can be seen in Ref. [11–13]. For completeness of the  
280 present paper, only the essential steps are highlighted here. The soot sampling experiment  
281 involves placing a probe in-parallel to the spray axis to skim the gas containing soot from the  
282 spray flame while minimizing the flow disturbance to the other half of the spray flame. As  
283 the reacting flow passes the probe, soot particles are deposited onto the carbon-coated copper  
284 grid inside the probe via thermophoresis. The sampled soot particles correspond to the soot  
285 present at that position. Sampled soot particles at different locations along the spray axis can  
286 be obtained by repeating the experiment with the probe being at different locations along the  
287 spray axis. The sampled soot particles are then observed under a High-Resolution  
288 Transmission Electron Microscope (HR-TEM). The diameter of each primary soot particles is  
289 finally obtained by manually processing the TEM images.

290 In order to simulate the same sampling technique along the spray axis, Lagrangian  
291 particles which are  $\pm 1.5\text{mm}$  axially and  $\pm 0.5\text{mm}$  radially about the sampling locations are  
292 assumed to be deposited onto the sampler and thus, their information is recorded. Similar  
293 analysis was carried out in our previous work [32]. Information of the deposited Lagrangian  
294 particles, such as size, position, velocity, etc, are gathered from the start of ignition (SOI) to  
295 6.0ms after start of ignition (ASOI). The analysis of the information gathered on the  
296 individual Lagrangian particles is later carried out in subsequent sections to obtain the  
297 primary soot size distribution and study its relation to soot processes.

### 298 3.2.2 Primary soot size distribution

299 The effect of ambient oxygen and density on primary soot size distribution at the core of the  
300 spray jet for the *n*-heptane spray cases are investigated here. The probability density function  
301 (PDF) of primary soot size for various ambient oxygen level and density cases are shown in  
302 Figure 5. It is observed that the onset location of soot moves downstream as oxygen level  
303 decreases. Soot is present at  $x = 50$  mm for the 15% O<sub>2</sub>, low density case, while soot is only  
304 present further downstream at  $x = 60$  mm for the 12% O<sub>2</sub>, low density case. This  
305 phenomenon is similarly captured for the high density case (not shown in the figure). The  
306 variation of soot onset location with oxygen level coincides with the experimental  
307 observation in [58–60] and in Section 3.1.3. Furthermore, Figure 5 also shows that in all the  
308 cases the primary soot diameters increase as soot particles migrate downstream. This is  
309 caused by the soot undergoing surface growth process and is consistent with experimental  
310 observations [8,9,18]

311 The mean primary soot diameter is computed from the collected Lagrangian particles  
312 along the core of the spray jet from the SOI to 6.0 ms ASOI and is shown in Figure 6. The  
313 mean primary soot size predicted at the oxygen level of 15% and ambient density of 30 kg/m<sup>3</sup>  
314 is in reasonable agreement with the measured mean primary soot size using *n*-dodecane fuel  
315 [61]. For the low density case, the mean primary soot size reaches a peak value of  
316 approximately 4.5 nm and 3.2 nm for oxygen levels of 15% and 12%, respectively. As  
317 ambient density increases to 30.0 kg/m<sup>3</sup>, the peak value of the predicted mean primary soot  
318 size also increases to 6.2 nm and 4.5 nm for oxygen levels of 15% and 12%, respectively.  
319 This implies that the increase in density resulted in the primary soot size to increase by a  
320 factor of 1.5. Furthermore, it is also evidently shown in Figure 6 that the mean primary soot  
321 size decreases with decreasing oxygen levels. There have been no experimental studies on the  
322 effects of ambient oxygen and density on primary soot size in diesel spray flame for *n*-

323 heptane fuel. However, experimental studies on SVF have shown that decreasing ambient  
324 oxygen [58] and increasing ambient density [62] can increase SVF in diesel spray flame. In  
325 addition, measurement of primary soot size in canonical flame setups also showed similar  
326 findings regarding the effect of oxygen [63] and ambient density [64–66] on primary soot  
327 sizes.

328         The results presented in Figures 5 and 6 are time-integrated results of all the collected  
329 Lagrangian particles along the core of the spray jet from the SOI to 6.0 ms ASOI. In order to  
330 gain a better insight on the effect of ambient oxygen and density on the primary soot size, the  
331 instantaneous primary soot size and the corresponding net growth rates experienced by the  
332 soot particles are analysed next. The temporal evolution of the net growth rates for all the  
333 cases are presented in Figure 7. Moreover, their corresponding evolution of the primary soot  
334 size distribution with respect to axial distance is presented in Figure 8.

335         At low density ( $14.8 \text{ kg/m}^3$ ), the maximum net growth rates for the 15%  $\text{O}_2$  and 12%  
336  $\text{O}_2$  cases are  $1 \times 10^5 \text{ kg/m}^3/\text{s}$  and  $0.25 \times 10^5 \text{ kg/m}^3/\text{s}$ , respectively. The span of soot cloud for the  
337 12%  $\text{O}_2$  case is shorter than the 15%  $\text{O}_2$  case from 1.0 ms ASOI to the steady-state period, as  
338 depicted in Figures 7(a) – (d). The evolution of the primary soot size is shown in Figure 8 to  
339 correspond to the net growth rates for the 15%  $\text{O}_2$  and 12%  $\text{O}_2$  cases, where a larger soot size  
340 is achieved in the former case due to having higher net growth rates.

341         At high density, the net growth rates for the 15%  $\text{O}_2$  case is higher than the 12%  $\text{O}_2$   
342 case (cf. Figure 7). Contrary to the low density case, the span of soot cloud at both oxygen  
343 levels are comparable to one another during the early ignition stage ( $t \leq 2 \text{ ms ASOI}$ ).  
344 However, the span of soot cloud for 12%  $\text{O}_2$  case becomes longer than the 15%  $\text{O}_2$  case at  
345 later times ( $t \geq 3 \text{ ms ASOI}$ ). During steady-state period, the span of soot cloud for the 12%  
346  $\text{O}_2$  is 10 mm longer than the 15%  $\text{O}_2$  case. The evolution of primary soot size at high density



347 shows similar trend to the ones at low density, where the primary soot size is larger for the  
348 15% O<sub>2</sub> (cf. Figure 8). In addition, increasing ambient density while keeping the ambient  
349 oxygen constant leads to an increase in primary soot sizes. This is likely due to the higher net  
350 growth rate achieved at higher ambient density, as depicted in Figure 7.

### 351 3.2.3 Soot age distribution

352 As the previous section has clearly demonstrated that the soot cloud span varies with different  
353 ambient conditions, it is expected that the longer span of the soot cloud would imply longer  
354 soot residence time in the spray flame. The use of the LST model allows the ability to analyse  
355 the residence time of soot in the spray flame by tracking the soot particles from the time of  
356 formation to the time of oxidation. The time duration of the soot particle from formation till  
357 oxidation is henceforth known as soot age [67]. It is important to note that the transient  
358 analysis of soot age is carried out after soot onset (ASO), where the soot onset time and onset  
359 location are tabulated in Table 3. The soot onset time is defined here as the earliest time after  
360 SOI when the total number of Lagrangian soot particles present in the domain are more than  
361 100 particles. The soot onset location is taken as the axial distance from the nozzle to the  
362 point where the maximal SVF is present, at the soot onset time. From Table 3, it is shown  
363 that the soot onset time and location increase as oxygen level decreases at both ambient  
364 densities. Shorter soot onset time and a more upstream soot onset location are obtained when  
365 the ambient density increases. These results agree qualitatively with the experimental and  
366 numerical findings in [59] which uses *n*-dodecane as fuel.

367 Figure 9 shows the predicted temporal evolution of soot age distribution of the  
368 primary soot particles at the core of spray jet with different ambient oxygen levels and  
369 densities. From 1.0 ms to 3.0 ms ASO, the soot age distributions at different oxygen levels  
370 and ambient densities are similar to one another. A narrower distribution is obtained for the  
371 15% O<sub>2</sub> case at high density as compared to the other cases at 4.0 ms ASO, which implies

372 that the soot particles in the 15% O<sub>2</sub>, high density case have a relatively shorter soot age than  
373 the other cases.

374 It is mentioned in Section 3.2.2 that the cloud span for the 12% O<sub>2</sub>, low density case is  
375 shorter than the 15% O<sub>2</sub>, low density case before reaching the steady-state period. Despite  
376 having a shorter soot cloud span, the soot age distribution in Figure 9 shows no significant  
377 difference between both oxygen level cases. This can be explained by the difference in the  
378 soot onset location in both cases. As mentioned earlier, the soot onset location for 15% O<sub>2</sub>,  
379 low density case is more upstream than the 12% O<sub>2</sub> case (as shown in Table 3). As the soot  
380 particles are formed nearer to the nozzle, the flow velocity experienced by the soot particles  
381 is higher than the ones further downstream. Therefore, the time taken to travel along the  
382 spray flame is shorter. Meanwhile, the soot onset location for the 12% O<sub>2</sub> case is further  
383 downstream. The lower flow velocity experienced by the soot particles consequently lead to  
384 particles travelling more slowly through the spray flame.

385 As for the high density case, the 15% O<sub>2</sub> case has a much narrower soot age  
386 distribution at 4.0 ms ASO cf. Figure 9(d) and a shorter soot cloud span than the 12% O<sub>2</sub> case  
387 at the steady-state period cf. Figure 8(h). This observation can also be attributed to the soot  
388 onset location. The soot onset location for both oxygen levels are close to one another, as  
389 shown in Table 3. This implies that the flow velocities experience by the soot particles at  
390 both oxygen levels are not significantly different. Therefore, the shorter soot cloud span in  
391 the 15% O<sub>2</sub> case would yield shorter soot age as what is predicted in Figure 9(d). The results  
392 above also show that longer soot cloud span does not necessary equate to longer soot  
393 residence time. The residence time of the soot particles in a spray flame is dependent on both  
394 the soot cloud span and the soot onset location.

#### 395 **4. Conclusion**

396 The effect of ambient oxygen level and density on the prediction of soot volume fraction and  
397 soot size distribution are carried out using a Lagrangian soot tracking method on Sandia *n*-  
398 heptane spray cases. The simulated SVF for the 12% O<sub>2</sub>, 30.0 kg/m<sup>3</sup> density case is  
399 underpredicted by approximately 30% relative to the measured data. At low density, the  
400 predicted SVF at 15% O<sub>2</sub> is overpredicted by a factor of two. Despite these discrepancies, the  
401 qualitative trend of the measured SVF where the SVF increases with increasing oxygen level  
402 and ambient density is captured by the simulated SVF.

403 The peak primary soot size achieved in the core of the spray jet at an ambient density  
404 of 14.8 kg/m<sup>3</sup> and oxygen level of 15% and 12% are 14 nm and 10 nm, respectively. Based  
405 on the primary soot size distribution in the core of the spray jet, an increase in ambient  
406 density from 14.8 kg/m<sup>3</sup> to 30 kg/m<sup>3</sup> is shown to increase the peak and mean primary soot  
407 size by a factor of 1.5. Furthermore, the peak and mean primary soot size decrease with  
408 decreasing oxygen levels from 15% to 12%. Higher oxygen level and ambient density lead to  
409 higher net growth rate experience by the soot particles, resulting in larger primary soot sizes.  
410 At low density, the soot cloud span is shorter for the 12% O<sub>2</sub> case as compared to the 15% O<sub>2</sub>  
411 case. On the contrary, the high density cases show comparable soot cloud span for both  
412 oxygen levels before steady-state period. With the introduction of soot age, the present study  
413 shows that longer span of the soot cloud does not equate to longer soot residence time in the  
414 spray flame.

415 Despite having different soot cloud span, the soot age distributions at different oxygen  
416 levels and ambient densities are similar to one another from 1.0 ms to 4.0 ms after soot onset  
417 time. The reason for this is likely due to the soot onset location. Soot particles that form  
418 upstream of the spray will experience higher flow velocity, thus leading to a shorter soot age  
419 when the span of the soot cloud is short.

420 **References**

- 421 [1] Chen L, Liang Z, Zhang X, Shuai S. Characterizing particulate matter emissions from  
422 GDI and PFI vehicles under transient and cold start conditions. *Fuel* 2017;189:131–  
423 40.
- 424 [2] Liu H, Ma X, Li B, Chen L, Wang Z, Wang J. Combustion and emission  
425 characteristics of a direct injection diesel engine fueled with biodiesel and  
426 PODE/biodiesel fuel blends. *Fuel* 2017;209:62–8.
- 427 [3] Kazemimanesh M, Moallemi A, Olfert JS, Kostiuk LW. Probe sampling to map and  
428 characterize nanoparticles along the axis of a laminar methane jet diffusion flame. *Proc*  
429 *Combust Inst* 2017;36:881–8.
- 430 [4] Bockhorn H. *Combustion Generated Fine Carbonaceous Particles: Proceedings of an*  
431 *International Workshop Held in Villa Orlandi, Anacapri, May 13-16, 2007*. KIT  
432 Scientific Publishing; 2009.
- 433 [5] Schwartz J. Air pollution and daily mortality: a review and meta analysis. *Environ Res*  
434 1994;64:36–52.
- 435 [6] European Parliament, Council of the European Union. **REGULATION (EC) No**  
436 **715/2007 OF THE EUROPEAN PARLIAMENT AND OF THE COUNCIL of 20**  
437 **June 2007 on type approval of motor vehicles with respect to emissions from light**  
438 **passenger and commercial vehicles (Euro 5 and Euro 6) and on access to vehicle repair**  
439 **and mai. Off J Eur Union 2007;L171:1–16. doi:OJEU 29.6.2007 L171.**
- 440 [7] Le Coq L. Élimination Des Particules. *Tech l’Ingénieur* 2006;33:20.
- 441 [8] Kook S, Pickett LM. Soot volume fraction and morphology of conventional and  
442 surrogate jet fuel sprays at 1000-K and 6.7-MPa ambient conditions. *Proc Combust*  
443 *Inst* 2011;33:2911–8.
- 444 [9] Yamaguchi T, Kondo K, Nishigai H, Takano S, Aizawa T. Direct Sampling, TEM

- 445 analysis and optical measurement of soot particles at different axial locations in a  
446 transient spray flame. *SAE Int J Fuels Lubr* 2011;5:316–28.
- 447 [10] Kondo K, Yamaguchi T, Nishigai H, Takano S, Aizawa T. High-Resolution  
448 Transmission Electron Microscopy of soot directly sampled at different axial locations  
449 in diesel spray Flame, No. 2011-24-0068, SAE Technical Paper, 2011.
- 450 [11] Aizawa T, Nishigai H, Kondo K, Yamaguchi T, Nerva JG, Genzale C, Kook S, Pickett  
451 L. Transmission electron microscopy of soot particles directly sampled in diesel spray  
452 flame - a comparison between US#2 and biodiesel soot. *SAE Int J Fuels Lubr*  
453 2012;5:665–73. doi:10.4271/2012-01-0695.
- 454 [12] Aizawa T, Takahata N, Okabe K, Mizutani Y. Effect of fuel aromatics on in-flame  
455 diesel soot nanostructure via HRTEM. No. 2015-01-1829. SAE Technical Paper; 2015.
- 456 [13] Kuribayashi M, Ishizuka Y, Aizawa T. Sizing of soot particles in diesel spray flame-a  
457 qualitative comparison between TEM analysis and LII/scattering laser measurements.  
458 *SAE Int J Fuels Lubr* 2013; 6(3):641-50.
- 459 [14] Kuribayashi M, Mizutani Y, Ishizuka Y, Taki N, Aizawa T. Effects of ambient oxygen  
460 concentration on soot processes in diesel spray flame-A qualitative comparison  
461 between TEM analysis and LII/Scattering laser measurements. *SAE Int J Fuels Lubr*  
462 2014;7:693–703.
- 463 [15] Kook S, Zhang R, Szeto K, Pickett LM, Aizawa T. In-flame soot sampling and particle  
464 analysis in a diesel engine. *SAE Int J Fuels Lubr* 2013;6:80–97. doi:10.4271/2013-01-  
465 0912.
- 466 [16] Zhang R, Kook S. Structural evolution of soot particles during diesel combustion in a  
467 single-cylinder light-duty engine. *Combust Flame* 2015;162:2720–8.
- 468 [17] Wang Y, Liu H, Li T, Jiang H, He P, Liu D, Zhang J, Xiong Q, Liu L. Characterization  
469 of the morphology and nanostructure of the soot particles produced within transient

- 470 diesel reacting jet flame by using thermophoretic sampling technique. *Energy & Fuels*  
471 2019;33:9124–37.
- 472 [18] Nerva JG, Yamaguchi T, Iguma H, Nishigai H, Kondo K, Takano S, Aizawa T,  
473 Genzale CL, Pickett LM. Transmission electron microscopy of soot particles sampled  
474 directly from a biodiesel spray flame. *SAE Int J Fuels Lubr* 2011;5:2011-01–2046.  
475 doi:10.4271/2011-01-2046.
- 476 [19] Sakai M, Iguma H, Kondo K, Aizawa T. Nanostructure analysis of primary soot  
477 particles directly sampled in diesel spray flame via HRTEM. No. 2012-01-1722. *SAE*  
478 *Technical Paper*; 2012.
- 479 [20] Jiang H, Li T, Wang Y, He P, Wang B. The evolution of soot morphology and  
480 nanostructure along axial direction in diesel spray jet flames. *Combust Flame*  
481 2019;199:204–12.
- 482 [21] Frenklach M. Method of moments with interpolative closure. *Chem Eng Sci*  
483 2002;57:2229–39.
- 484 [22] Mueller ME, Blanquart G, Pitsch H. A joint volume-surface model of soot aggregation  
485 with the method of moments. *Proc Combust Inst* 2009;32:785–92.
- 486 [23] Ito T, Hosaka T, Ueda M, Senda J, Fujimoto H. Detailed kinetic modeling and laser  
487 diagnostics of soot formation process in diesel jet flame. *SAE Transactions*.  
488 2004;1:602-13.
- 489 [24] Naik CV, Puduppakkam KV, Meeks E. Simulation of soot volume fraction and size in  
490 high-pressure lifted flames using detailed reaction mechanisms. *ASME Turbo Expo*  
491 2014 Turbine Tech Conf Expo 2014:V04BT04A025.
- 492 [25] Gelbard F, Seinfeld JH. Simulation of multicomponent aerosol dynamics. *J Colloid*  
493 *Interface Sci* 1980;78:485–501.
- 494 [26] Gelbard F, Tambour Y, Seinfeld JH. Sectional representations for simulating aerosol

495 dynamics. *J Colloid Interface Sci* 1980;76:541–56.

496 [27] Pope CJ, Howard JB. Simultaneous particle and molecule modeling (SPAMM): An  
497 approach for combining sectional aerosol equations and elementary gas-phase  
498 reactions. *Aerosol Sci Technol* 1997;27:73–94.

499 [28] Aubagnac-Karkar D, Michel J-B, Colin O, Noël L, Darabiha N. A Sectional Soot  
500 Model for RANS Simulation of Diesel Engines. SAE Technical Paper; 2014.

501 [29] Aubagnac-Karkar D, Michel J-B, Colin O, Vervisch-Kljakic PE, Darabiha N.  
502 Sectional soot model coupled to tabulated chemistry for Diesel RANS simulations.  
503 *Combust Flame* 2015;162:3081–99.

504 [30] Gallen L, Felden A, Riber E, Cuenot B. Lagrangian tracking of soot particles in LES  
505 of gas turbines. *Proceedings of the Combustion Institute*. 2019 Jan 1;37(4):5429-36.

506 [31] Dellinger N, Bertier N, Dupoirieux F, Legros G. Hybrid Eulerian-Lagrangian method  
507 for soot modelling applied to ethylene-air premixed flames. *Energy*. 2020 Mar  
508 1;194:116858.

509 [32] Ong JC, Pang KM, Walther JH, Ho J-H, Ng HK. Evaluation of a Lagrangian soot  
510 tracking method for the prediction of primary soot particle size under engine-like  
511 conditions. *J Aerosol Sci* 2018;115:70–95.

512 [33] Weller HG, Tabor G, Jasak H, Fureby C. A tensorial approach to computational  
513 continuum mechanics using object-oriented techniques. *Comput Phys* 1998;12:620–  
514 31.

515 [34] ECN. Engine Combustion Network 2020. [www.sandia.gov/ecn/](http://www.sandia.gov/ecn/).

516 [35] Reitz RD, Diwakar R. Effect of drop breakup on fuel sprays. *SAE Transactions*.  
517 1986;1:218-27.

518 [36] Launder BE, Spalding DB. The numerical computation of turbulent flows. *Comput*  
519 *Methods Appl Mech Eng* 1974;3:269–89. doi:<https://doi.org/10.1016/0045->

520 7825(74)90029-2.

521 [37] Novella R, García A, Pastor JM, Domenech V. The role of detailed chemical kinetics  
522 on CFD diesel spray ignition and combustion modelling. *Math Comput Model*  
523 2011;54:1706–19.

524 [38] Pang KM, Jangi M, Bai X-S, Schramm J. Investigation of chemical kinetics on soot  
525 formation event of n-heptane spray combustion. No. 2014-01-1254. SAE Technical  
526 Paper; 2014.

527 [39] Pang KM, Jangi M, Bai X-S, Schramm J. Evaluation and optimisation of  
528 phenomenological multi-step soot model for spray combustion under diesel engine-  
529 like operating conditions. *Combust Theory Model* 2015;19:279–308.

530 [40] Varna A, Wehrfritz A, Hawkes ER, Cleary MJ, Lucchini T, D’Errico G, Kook S, Chan  
531 QN. Application of a multiple mapping conditioning mixing model to ECN Spray A.  
532 *Proceedings of the Combustion Institute*. 2019 Jan 1;37(3):3263-70.

533 [41] Skeen S, Manin J, Pickett L, Dalen K, Ivarsson A. Quantitative spatially resolved  
534 measurements of total radiation in high-pressure spray flames. No. 2014-01-1252.  
535 SAE Technical Paper; 2014.

536 [42] Jangi M, D’Errico G, Bai X-S, Lucchini T. Numerical simulation of the ECN Spray A  
537 using multidimensional chemistry coordinate mapping: n-dodecane diesel combustion.  
538 No. 2012-01-1660. SAE Technical Paper; 2012.

539 [43] Ranz WE, Marshall WR. Evaporation from drops. *Chem Eng Prog* 1952;48:141446.

540 [44] Frossling N. Evaporation, heat transfer, and velocity distribution in two-dimensional  
541 and rotationally symmetrical laminar boundary-layer flow. DTIC Document; 1956.

542 [45] Pang KM, Ng HK, Gan S. Development of an integrated reduced fuel oxidation and  
543 soot precursor formation mechanism for CFD simulations of diesel combustion. *Fuel*  
544 2011;90:2902–14.



- 545 [46] Kitanidis PK. Particle-tracking equations for the solution of the advection-dispersion  
546 equation with variable coefficients. *Water Resour Res* 1994;30:3225–7.
- 547 [47] Zhang Z, Chen Q. Comparison of the Eulerian and Lagrangian methods for predicting  
548 particle transport in enclosed spaces. *Atmos Environ* 2007;41:5236–48.
- 549 [48] Bolla M, Wright YM, Boulouchos K, Borghesi G, Mastorakos E. Soot formation  
550 modeling of n-heptane sprays under diesel engine conditions using the conditional  
551 moment closure approach. *Combustion Science and Technology*. 2013 May  
552 4;185(5):766-93.
- 553 [49] Haynes BS, Wagner HG. The surface growth phenomenon in soot formation.  
554 *Zeitschrift für Physikalische Chemie*. 1982 Feb 1;133(2):201-13.
- 555 [50] Brookes SJ, Moss JB. Predictions of soot and thermal radiation properties in confined  
556 turbulent jet diffusion flames. *Combust Flame* 1999;116:486–503.
- 557 [51] Ong, JC, Development of Lagrangian soot tracking method for the study of soot  
558 morphology in diesel spray combustion. PhD Thesis. University of Nottingham, 2017.
- 559 [52] Leung KM, Lindstedt RP, Jones WP. A simplified reaction mechanism for soot  
560 formation in nonpremixed flames. *Combust Flame* 1991;87:289–305.
- 561 [53] Vishwanathan G, Reitz RD. Development of a practical soot modeling approach and  
562 its application to low-temperature diesel combustion. *Combust Sci Technol*  
563 2010;182:1050–82.
- 564 [54] Katta VR, Blevins LG, Roquemore WM. Dynamics of an inverse diffusion flame and  
565 its role in polycyclic-aromatic-hydrocarbon and soot formation. *Combust Flame*  
566 2005;142:33–5
- 567 [55] Pei Y, Som S, Pomraning E, Senecal PK, Skeen SA, Manin J, Pickett LM. Large eddy  
568 simulation of a reacting spray flame with multiple realizations under compression  
569 ignition engine conditions. *Combustion and Flame*. 2015 Dec 1;162(12):4442-55.

- 570 [56] Fernandez SF, Paul C, Sircar A, Imren A, Haworth DC, Roy S, Modest MF. Soot and  
571 spectral radiation modeling for high-pressure turbulent spray flames. *Combustion and*  
572 *Flame*. 2018 Apr 1;190:402-15.
- 573 [57] Chishty MA, Bolla M, Hawkes ER, Pei Y, Kook S. Soot formation modelling for n-  
574 dodecane sprays using the transported PDF model. *Combustion and Flame*. 2018 Jun  
575 1;192:101-19.
- 576 [58] Idicheria CA, Pickett LM. Soot formation in diesel combustion under high-EGR  
577 conditions. *SAE Transactions*. 2005;1:1559-74.
- 578 [59] Cenker E. Imaging measurements of soot particle size and soot volume fraction with  
579 laser-induced incandescence at Diesel engine conditions. Ph.D. Thesis., Ecole Centrale  
580 Paris, 2014.
- 581 [60] Pandurangi SS, Bolla M, Wright YM, Boulouchos K, Skeen SA, Manin J, Pickett LM.  
582 Onset and Progression of Soot in high-pressure n-Dodecane Sprays under Diesel-  
583 Engine Conditions. *Int J Engine Re*. 2017;18(5-6):436-52.
- 584 [61] Kook S, Zhang R, Chan QN, Aizawa T, Kondo K, Pickett LM, Cenker E, Bruneaux G,  
585 Andersson O, Pagels J, Nordin EZ. Automated detection of primary particles from  
586 transmission electron microscope (TEM) images of soot aggregates in diesel engine  
587 environments. *SAE Int J Engines* 2016;9:279–96.
- 588 [62] Pickett LM, Siebers DL. Soot in diesel fuel jets: effects of ambient temperature,  
589 ambient density, and injection pressure. *Combust Flame* 2004;138:114–35.
- 590 [63] Oh KC, Shin HD. The effect of oxygen and carbon dioxide concentration on soot  
591 formation in non-premixed flames. *Fuel* 2006;85:615–24.
- 592 [64] Vargas AM, Gülder ÖL. Pressure dependence of primary soot particle size determined  
593 using thermophoretic sampling in laminar methane-air diffusion flames. *Proc Combust*  
594 *Inst* 2017;36:975–84.

- 595 [65] Amin HMF, Roberts WL. An experimental apparatus to measure soot morphology at  
596 high pressures using multi-angle light scattering. *Meas Sci Technol* 2019;30:75902.
- 597 [66] Amin HMF, Roberts WL. Investigating soot parameters in an ethane/air counterflow  
598 diffusion flame at elevated pressures. *Combust Sci Technol* 2020:1–16.
- 599 [67] Singh J, Balthasar M, Kraft M, Wagner W. Stochastic modeling of soot particle size  
600 and age distributions in laminar premixed flames. *Proc Combust Inst* 2005;30:1457–  
601 65.
- 602

## List of Figures

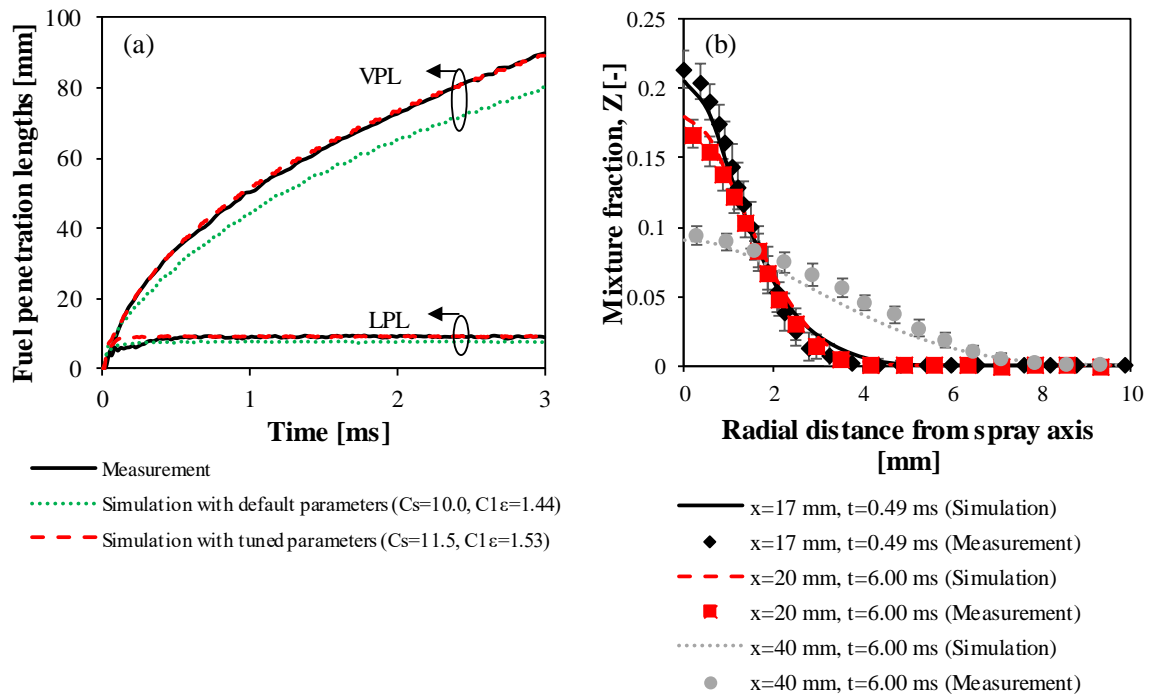


Figure 1: (a) Comparison of liquid and vapour penetration length for the non-reacting  $n$ -heptane spray case. (b) Comparison of simulated and experimental radial mixture fraction of the non-reacting  $n$ -heptane spray case at different axial locations and time after injection.

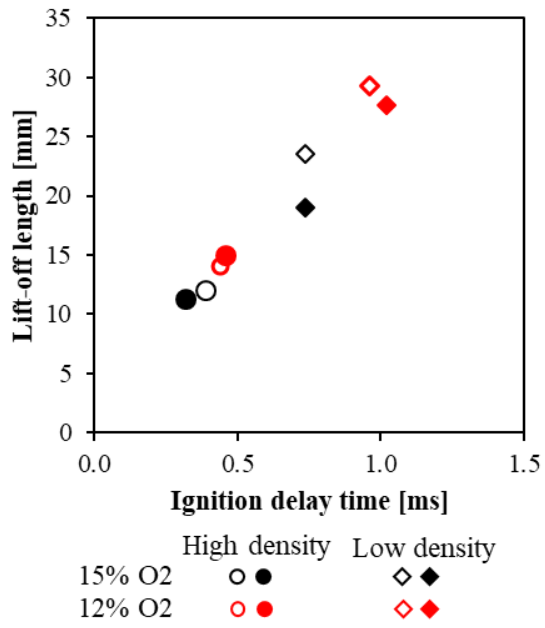


Figure 2: Comparison of simulated ignition delay time (IDT) and lift-off length (LOL) for the reacting *n*-heptane spray cases with experimental results at different ambient oxygen levels and ambient densities. [Hollow symbols represent measured data; Filled symbols represent simulation data]

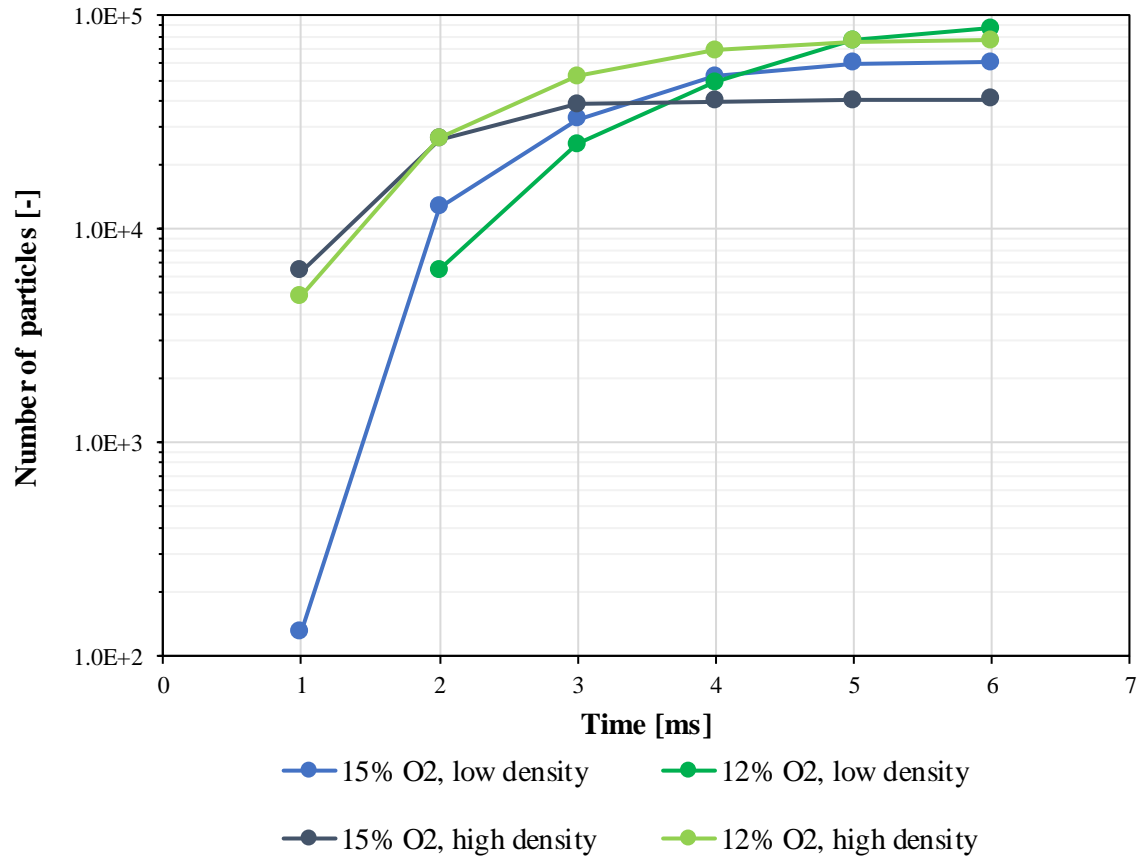


Figure 3: Temporal evolution of the number of computational particles for soot under different ambient densities and oxygen levels.

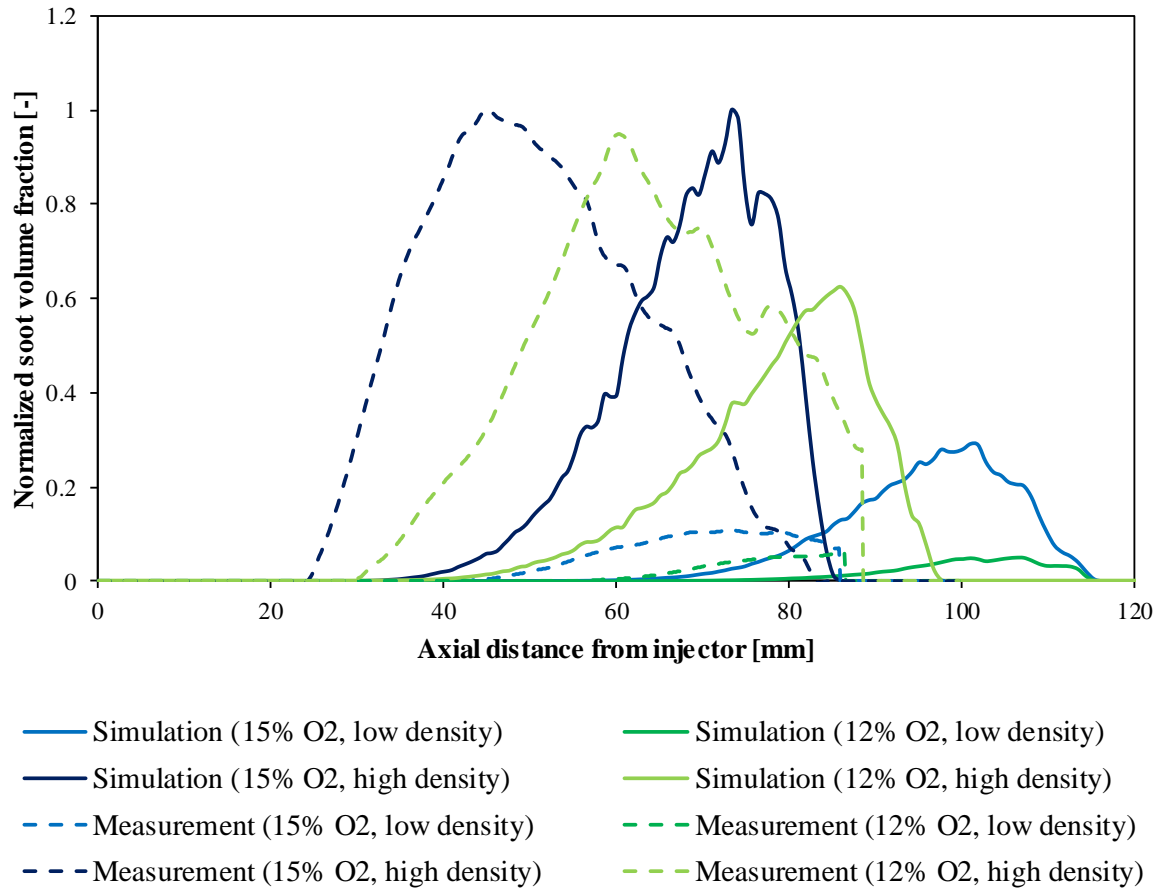


Figure 4: Normalized SVF as a function of the axial distance from injector for 15% and 12% oxygen levels at ambient density of  $14.8 \text{ kg/m}^3$  (low density) and  $30.0 \text{ kg/m}^3$  (high density).

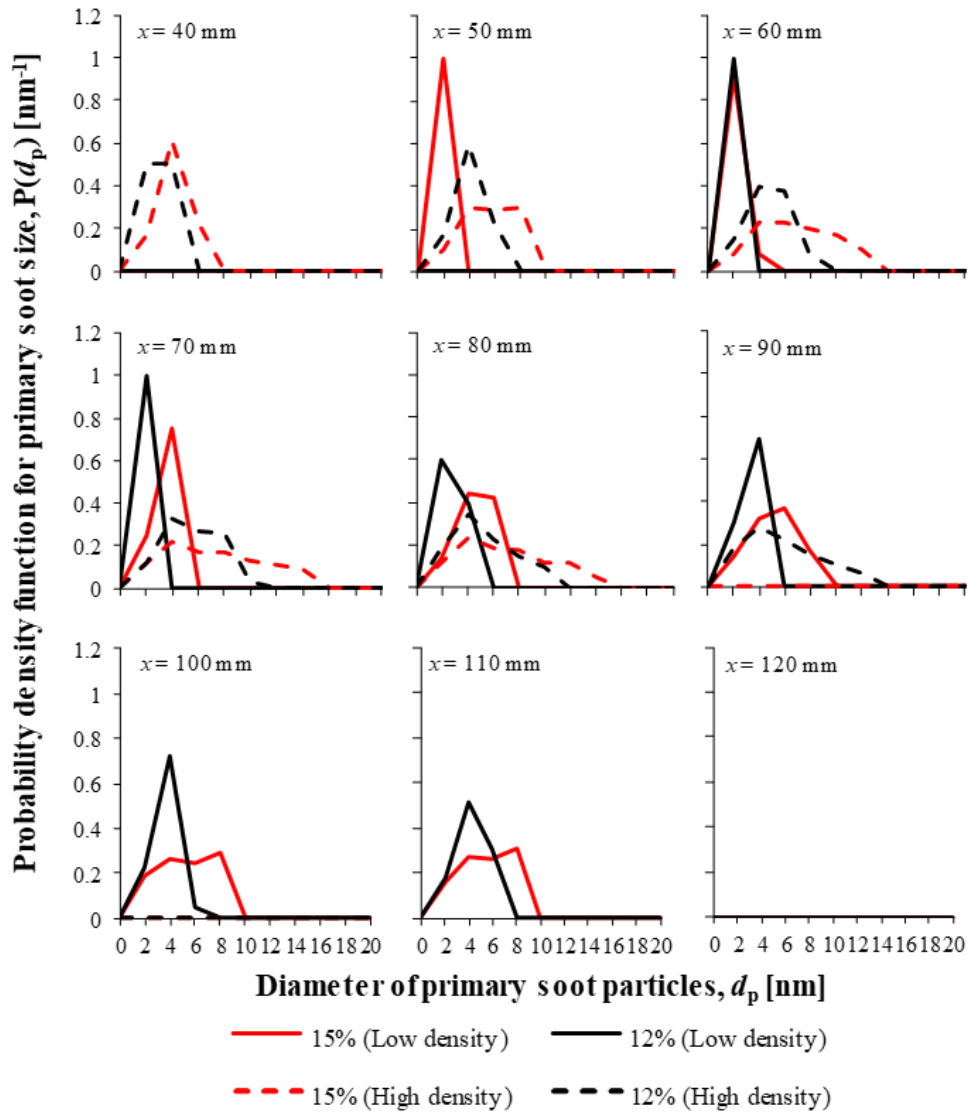


Figure 5: Probability density function (PDF) of primary soot size predicted along various axial locations from injector location for different ambient oxygen level and density cases.



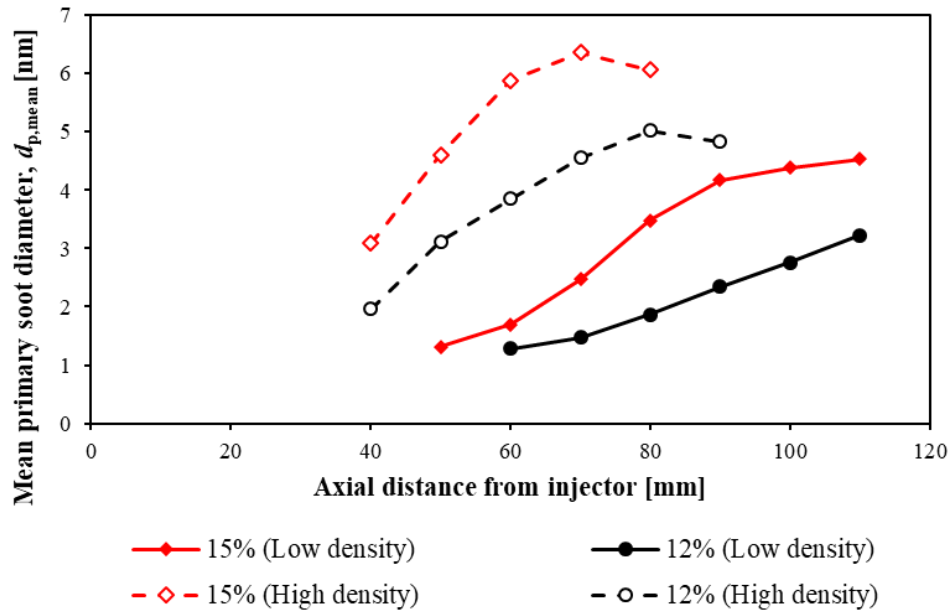


Figure 6: Mean primary soot size as a function of axial distance from injector for different ambient oxygen level and density cases. The filled symbols refer to low density cases; hollow symbols refer to high density cases.

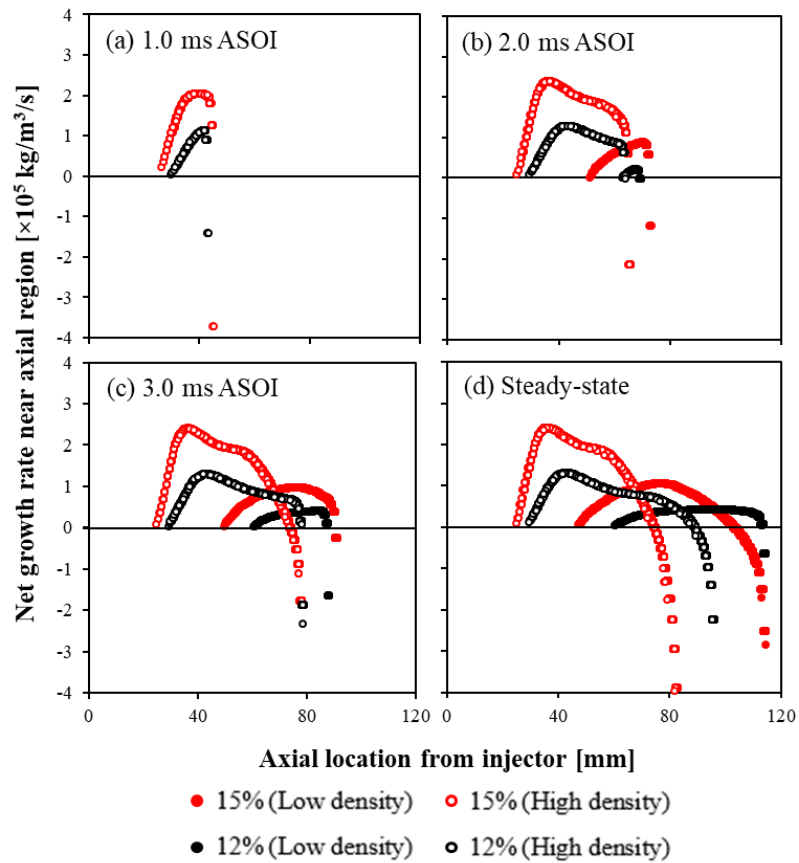


Figure 7: Temporal evolution of the net growth rates at core of spray jet for different ambient oxygen level and density cases at different timings. The filled symbols refer to low density cases; hollow symbols refer to high density cases.

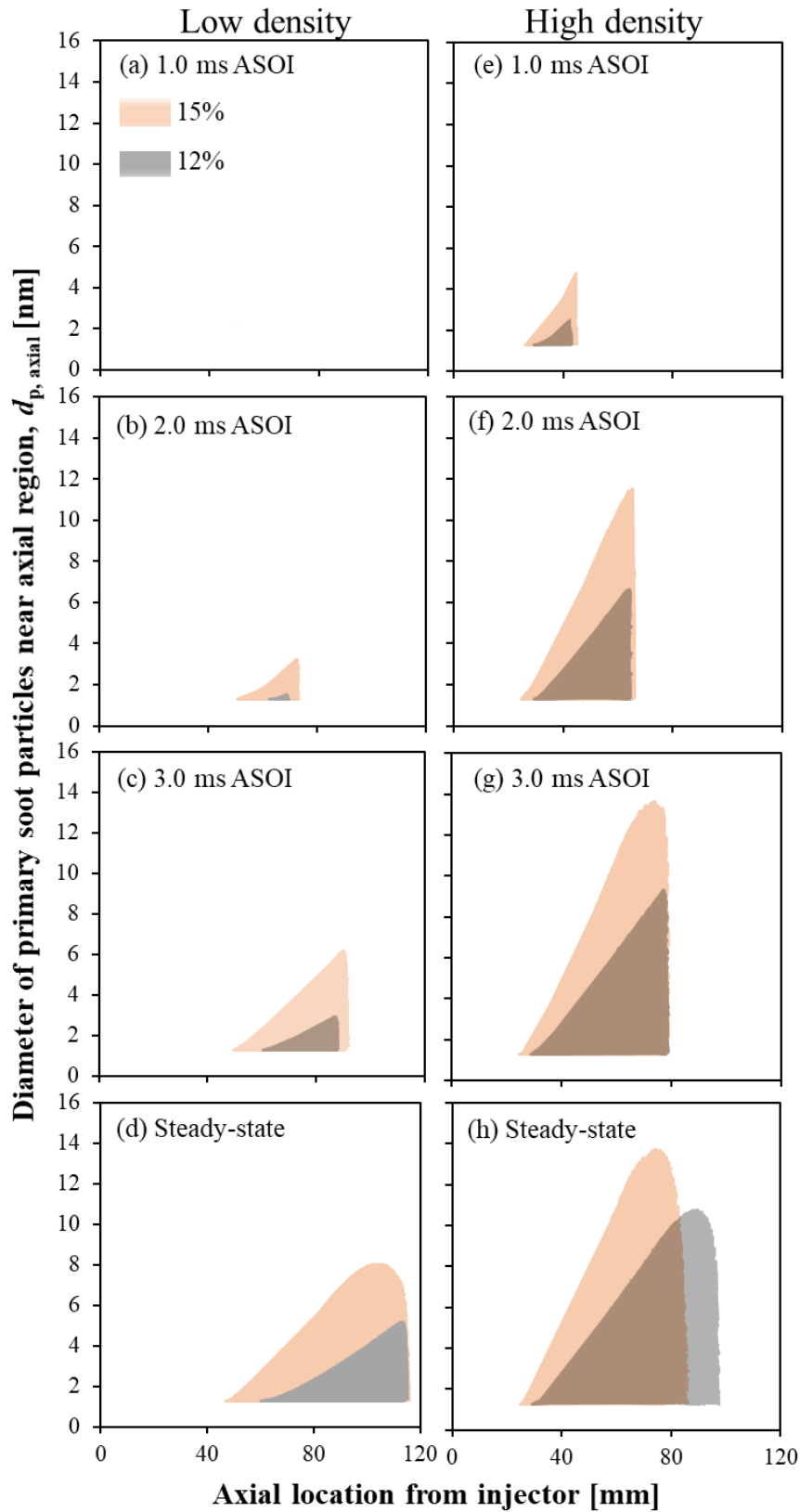


Figure 8: Primary soot size distribution at the core of the spray jet for different ambient oxygen level and density cases. (a) – (d) refer to low density cases and (e) – (f) refer to high density cases.

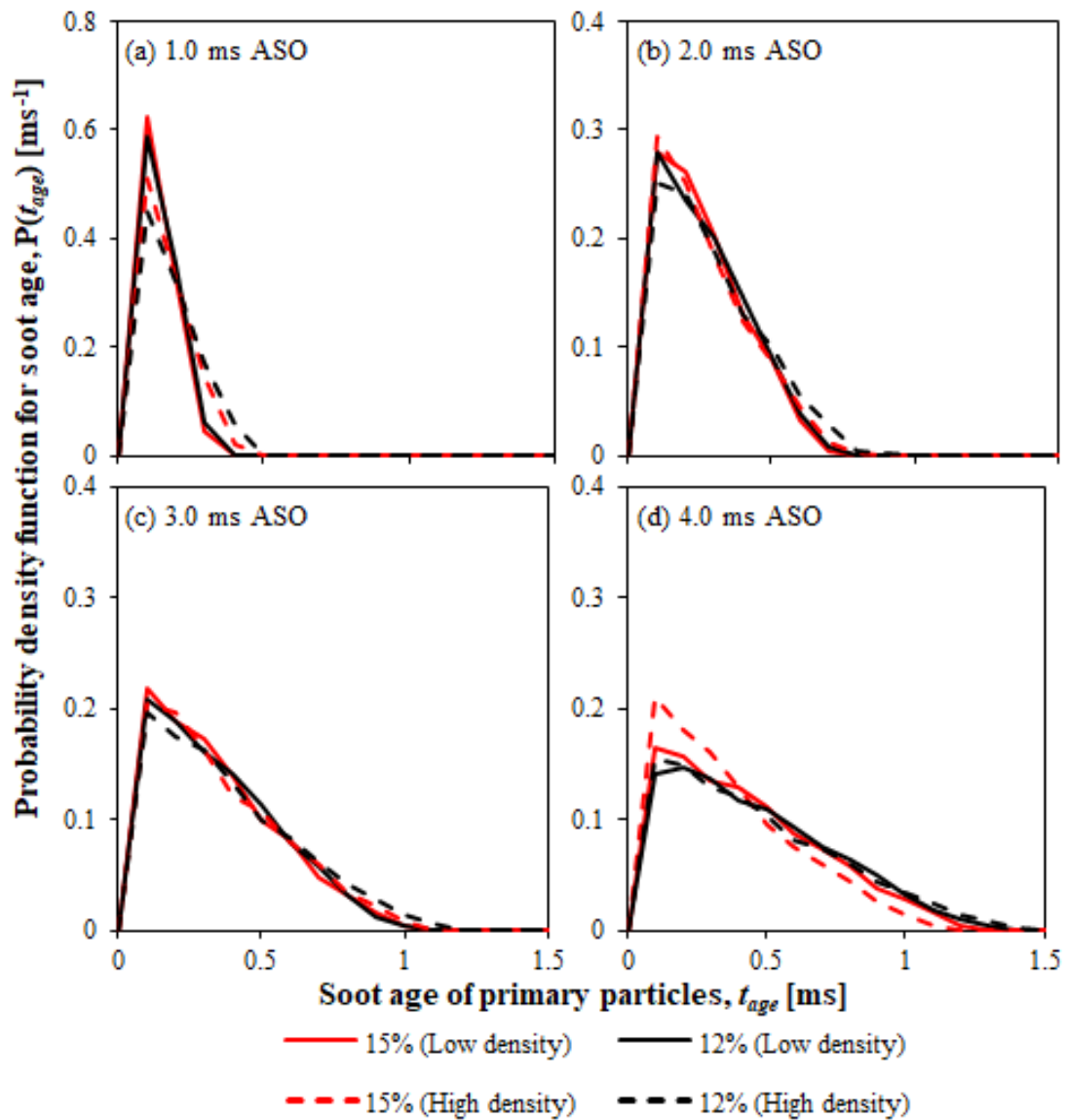


Figure 9: Soot age distribution of soot particles at the core of spray jet for different ambient oxygens and densities at different timing ASO. Solid lines refer to low density cases; dashed lines refer to high density cases.

## List of Tables

Table 1: Experimental conditions for Sandia *n*-heptane test cases. Data taken from Ref. [34].

Spray configuration	$T_{am}$ [K]	$\rho_{am}$ [kg/m <sup>3</sup> ]	O <sub>2</sub> % [-]	Injection duration [ms]	Nozzle orifice diameter [mm]	Injection pressure drop [MPa]	Total fuel mass [mg]
Non-reacting	1000	14.8	0	6.8	0.1	150	17.8
Reacting	1000	14.8	15	6.8	0.1	150	17.8
			12	6.8	0.1	150	17.8
	1000	30.0	15	6.8	0.1	150	18.0
			12	6.8	0.1	150	17.8

$T_{am}$ : Ambient temperature ;  $\rho_{am}$ : Ambient density ; O<sub>2</sub> %: Ambient oxygen concentration (in mole fraction)

Table 2: The soot model constants. Data taken from Ref. [50,52]

Soot Model Constants	Descriptions	Value [Unit]
$C_{sg}$	Surface growth rate scaling factor	11,700 [kg m kmol <sup>-1</sup> s <sup>-1</sup> ]
$C_{OH}$	Model constant for soot oxidation due to OH	105.81 [kg m kmol <sup>-1</sup> K <sup>-0.5</sup> s <sup>-1</sup> ]
$C_{O_2}$	Model constant for soot oxidation due to O <sub>2</sub>	8903.51 [kg m kmol <sup>-1</sup> K <sup>-0.5</sup> s <sup>-1</sup> ]
$T_{sg}$	Activation temperature of surface growth	12,100 [K]
$T_{O_2}$	Activation temperature of soot oxidation due to O <sub>2</sub>	19,778 [K]
$\eta_{coll}$	Collision efficiency parameter	0.13 [-]

Table 3: Soot onset time and onset location for different ambient oxygen level and density *n*-heptane spray cases.

Ambient density [kg/m <sup>3</sup> ]	Ambient oxygen [%]	Soot onset time [ms]	Soot onset location [mm]
14.8	15	0.94	48
	12	1.38	58
30.0	15	0.41	27
	12	0.57	30